Magnetic structure and properties of $BiMn_2O_5$ oxide: A neutron diffraction study

A. Muñoz*
Departamento de Física Aplicada, EPS, Universidad Carlos III, Avenida Universidad, 30, Leganés-Madrid E-28911, Spain

J. A. Alonso, M. T. Casais, M. J. Martínez-Lope, and J. L. Martínez
Instituto de Ciencia de Materiales de Madrid, CSIC, Cantoblanco, E-28049 Madrid, Spain

M. T. Fernández-Díaz
Institut Laue Langevin, Boîte Postale 156X, Grenoble, F-38042, France
(Received 8 November 2001; published 29 March 2002)

$BiMn_2O_5$ has been prepared in polycrystalline form by a citrate technique, and studied by neutron powder diffraction (NPD), specific-heat, and magnetization measurements. High-resolution NPD data show that $BiMn_2O_5$ is orthorhombic (space group $Pbam$, $Z=4$) and contains infinite chains of $Mn^{4+}O_6$ octahedra sharing edges, linked together by $Mn^{3+}O_5$ pyramids and BiO_8 units. These units are strongly distorted with respect to those observed in other members of the RMn_2O_5 family (R denotes rare earths), due to the presence of the electronic lone pair on Bi^{3+}. $BiMn_2O_5$ becomes magnetically ordered below $T_N=39$ K. The magnetic structure, investigated from low-temperature NPD data, is defined by the propagation vector $\mathbf{k}=(1/2,0,1/2)$. A group theory analysis has been carried out to determine the possible solutions for the magnetic structure. For the Mn^{3+} ions located at the $4h$ site, the magnetic moments are ordered according to the basis vectors $(F_x,C_y,0)$; for the Mn^{4+} ions placed at the $4f$ site, the basis vectors are $(G'_x,A'_y,0)$. At $T=1.6$ K, the magnetic moments for Mn^{3+} and Mn^{4+} cations are $3.23(6)\mu_B$ and $2.51(7)\mu_B$, respectively. The commensurate character of the magnetic structure of $BiMn_2O_5$, in contrast with the incommensurate structure observed for other compounds of the RMn_2O_5 family, for which $\mathbf{k}=(1/2,0,k_z)$, is discussed in terms of competing antiferromagnetic interactions, depending on the observed variation of crucial Mn-O-Mn distances.

DOI: 10.1103/PhysRevB.65.144423 PACS number(s): 75.25.+z

I. INTRODUCTION

The discovery of a colossal magnetoresistance effect in the hole-doped rare-earth manganites $R_{1-x}A_xMnO_3$ (A denotes alkaline earth) (Refs. 1 and 2) has originated a great interest in the study of the manganese oxides, in general, and particularly in those containing a mixed valence for Mn cations. RMn_2O_5 (R stands for rare-earth metals, Y, and Bi) are included in this category. According to the first studies carried out in the 1960s to determine their crystallographic structure,[3,4] all the compounds of the RMn_2O_5 series crystallize in the orthorhombic space group $Pbam$. The manganese ions occupy two sites with different oxidation states. The Mn^{4+} ions ($4f$ site) are octahedrally coordinated to oxygens; the $Mn^{4+}O_6$ octahedra share edges to form infinite chains along the c axis. The Mn^{3+} ions ($4h$ site) are coordinated to five oxygens located at the apexes of a distorted tetragonal pyramid. The $Mn^{4+}O_6$ chains are interconnected by $Mn^{3+}O_5$ pyramids. The R^{3+} cations form RO_8 polyhedra. A bond-valence study from high-resolution neutron powder diffraction (NPD) data revealed the presence of important tensile and compressive stresses, which are progressively released along the series as the rare-earth metal size decreases.[5]

Regarding the magnetic properties of these compounds, some work has been devoted to the determination of their magnetic structures by neutron diffraction. According to the first reports,[6,7] these oxides present an antiferromagnetic (AFM) ordering below 40 K. For $R=$ Nd, Tb, Ho, Er, and Y, the magnetic structure is defined by the propagation vector $\mathbf{k}=(1/2,0,\tau)$. Both Mn ions are ordered according to a helicoidal arrangement with the moments in the ab plane. The R^{3+} cations order at lower temperatures with a sinusoidal magnetic structure. Subsequent results also showed for $R=$ Er and Tb (Ref. 8) that the amplitude of the moments for the Mn ions is modulated. The magnetic structure of $DyMn_2O_5$ was analyzed in detail;[9] it is defined by two propagation vectors $\mathbf{k}_1=(1/2,0,0)$ and $\mathbf{k}_2=(1/2,0,\tau)$. With respect to $BiMn_2O_5$, a propagation vector $\mathbf{k}=(1/2,01/2)$ was reported to define its magnetic ordering,[10] although no more details were given. On the other hand, the published results on the dielectric and magnetoelectric properties of RMn_2O_5 (Refs. 11–13) seem to indicate the possibility of ferroelectricity in these compounds.

The aim of this paper is to carry out a detailed study of the magnetic behavior of $BiMn_2O_5$, whose magnetic structure seems to be different from that of the remaining compounds of the series. A detailed crystallographic study from high-resolution neutron powder diffraction data, followed by a study of its magnetic structure and its evolution with temperature, are complemented with magnetization and specific-heat measurements.

II. EXPERIMENTAL

$BiMn_2O_5$ was obtained as a dark brown polycrystalline powder starting from precursors previously synthesized by a wet-chemistry technique. Stoichiometric amounts of analytical grade Bi_2O_3 and $Mn(NO_3)_2\cdot 4H_2O$ were solved in citric acid. The citrate solutions were slowly evaporated and de-

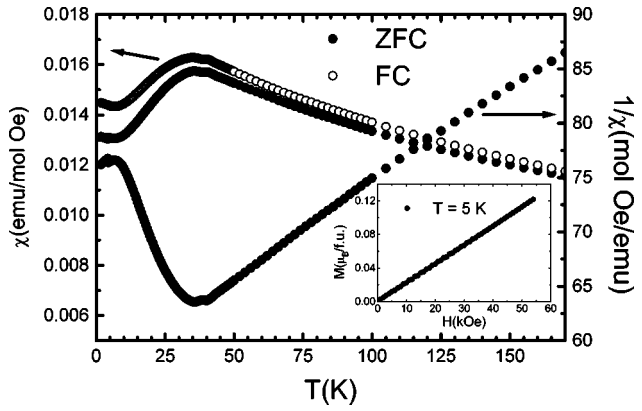

FIG. 1. Thermal evolution of the dc susceptibility and its reciprocal measured under a 0.5 kOe magnetic field in zero-field-cooling (ZFC) and field-cooling conditions. Inset: Isothermal magnetization curve at $T=5$ K.

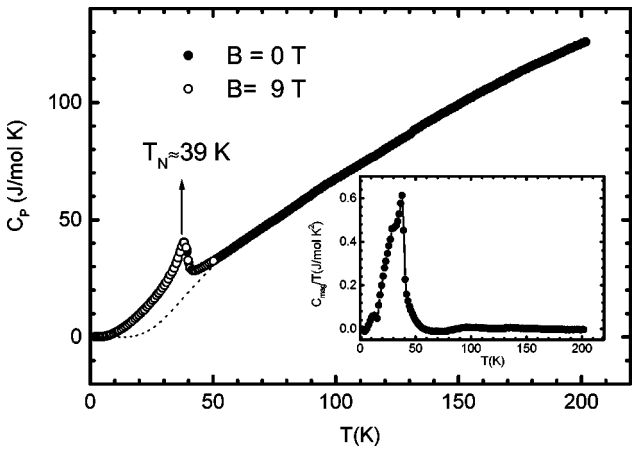

FIG. 2. Temperature dependence of the specific heat under zero and 9 T magnetic field. The dotted line represents the calculated lattice contribution. Inset: Thermal evolution of the magnetic contribution to the specific heat.

composed at temperatures up to 600 °C. All the organic materials were eliminated in a subsequent treatment at 800 °C in air. The sample was finally annealed at 1000 °C in air for 12 h.

X-ray powder diffraction patterns were collected with Cu $K\alpha$ radiation in a Siemens D-501 goniometer controlled by a DACO-MP computer. The magnetic measurements were carried out in a commercial superconducting quantum interference device magnetometer. The dc susceptibility measurements, both under zero-field-cooling (ZFC) and field-cooling (FC) conditions, were performed in a 0.5 kOe magnetic field for temperatures ranging from 1.8 K to 300 K. An isothermal magnetization curve was obtained at $T=5$ K in a magnetic field up to 54 kOe. The specific-heat measurements were carried out in a semiadabatic He calorimeter using the heat-pulsed method for temperatures going from 2 K to 200 K under a zero and 90 kOe magnetic field. A high-resolution NPD pattern was acquired at room temperature at the D2B diffractometer of the Institut Laue-Langevin in Grenoble (France), with a wavelength of 1.594 Å. The collection time for a 6-g sample was about 3 h. The magnetic structure and its thermal evolution was studied at the D1B multidetector (400 counters) diffractometer with a wavelength $\lambda=2.532$ Å. A good statistics pattern, collected in 30 min at 1.6 K, was used to resolve the magnetic structure. The thermal evolution was studied from sequential diagrams collected every 2 K, on heating from 1.6 K to 53 K, with a counting time of 10 min each. The refinements of the crystallographic and the magnetic structures were performed by using the Rietveld method with the FULLPROF program.[14] In the profile refinements, the peak shape was simulated by a pseudo-Voigt function and the background was fitted with a fifth-degree polynomial function.

III. RESULTS FROM MAGNETIC AND SPECIFIC-HEAT MEASUREMENTS

A. Magnetic measurements

The dependence of the magnetic susceptibility with temperature is presented in Fig. 1. At low temperatures, the susceptibility increases and exhibits an outspread maximum with two characteristic temperatures $T=39$ K and $T=36$ K, which would suggest the appearance of an AFM order with $T_N=39$ K. The existence of two transition temperatures could indicate a small delay in the ordering of the magnetic moments associated with one of the manganese sites with respect to the second one. The evolution of the ZFC and the FC curves is very similar, which seems to exclude the presence of weak ferromagnetism effects. This is also confirmed by the magnetization curve shown in the inset of Fig. 1, exhibiting a perfectly linear behavior with the magnetic field. Above 100 K the susceptibility follows a Curie-Weiss behavior (see Fig. 1) characterized by a paramagnetic temperature $\Theta_P=-357(3)$ K and with an effective paramagnetic moment of $6.9(1)\mu_B$. This figure is close to the theoretical value of $6.24\mu_B$ that has been calculated through the expression $P_{eff}=\sqrt{P_{eff}^2(Mn^{3+})+P_{eff}^2(Mn^{4+})}$.

B. Specific-heat measurements

The temperature evolution of specific heat under zero and $B=9$ T magnetic fields is shown in Fig. 2. A sharp anomaly appears at around the ordering temperature $T_N\approx 39$ K, in good agreement with the magnetic measurements. In the curves there are no differences between the measurements obtained in zero and 9 T magnetic fields. The low-temperature specific-heat data has been fitted by the expression

$$C=\gamma T+\beta T^3+BT^{\delta}. \tag{1}$$

The linear term is associated with the charge-carrier contribution, the βT^3 term corresponds to the lattice contribution, and the last term BT^{δ} is related to the spin-wave excitations. By considering the data from 2 K to 16 K, the best fit is obtained if the linear term is neglected and $\delta=2$, with the parameters $\beta=0.0012(1)$ J/mol K^4 and $B=0.0048(13)$ J/mol K^3. The Debye temperature Θ_D can be calculated from β through the expression

TABLE I. Structural parameters obtained after the Rietveld refinement of the high-resolution NPD pattern at 295 K with $\lambda = 1.594$ Å. Space group *Pbam*.

Atoms	Positions	*x*	*y*	*z*	*B* (Å)^2
Bi	4*g*	0.1597(2)	0.1659(1)	0.0000	0.40(2)
Mn1	4*f*	0.5000	0.0000	0.2613(4)	0.21(4)
Mn2	4*h*	0.4074(3)	0.3516(3)	0.5000	0.25(4)
O1	4*e*	0.0000	0.0000	0.2866(3)	0.60(3)
O2	4*g*	0.1553(2)	0.4440(2)	0.0000	0.34(3)
O3	4*h*	0.1440(2)	0.4241(2)	0.5000	0.33(3)
O4	8*i*	0.3856(1)	0.1995(1)	0.2539(2)	0.45(2)
Cell parameters	$a = 7.56078(8)$ Å, $b = 8.53299(8)$ Å, $c = 5.76066(5)$ Å				
Volume	$V = 371.654(6)$ Å^3				
Disc. factors		$R_p = 4.3\%$	$R_{wp} = 5.6\%$	$\chi^2 = 1.3$	

$\Theta_D = (12\pi^4 pR/5\beta)^{1/3}$, *R* being the gas constant and *p* the number of atoms per formula unit. The Debye temperature obtained in this way is $\Theta_D = 235(4)$ K. The quadratic term in the thermal behavior of the specific heat is characteristic of the AFM spin waves. The entropy associated with the magnetic transition can be determined through the expression $\Delta S = \int (C_{mag}/T) dT$. The magnetic contribution to the specific heat is extracted after evaluating the lattice contribution. The lattice contribution has been obtained by fitting the data to two Einstein optical modes, one associated with the Bi + Mn atoms and the other with the O atoms. The oscillator corresponding to the Bi + Mn atoms is centered at $\Theta_E = 172(1)$ K and the other at $\Theta_E = 648(1)$ K. The magnetic contribution is represented in the inset of Fig. 2, and the entropy change is 12.5 J/(mol K). This value is close to that expected for a mixture of free Mn^{3+} and Mn^{4+} ions, $\Delta S = 0.5R \ln(2S_1+1) + 0.5R \ln(2S_2+1) = 12.45$ J/mol K ($S_1 = 2$ for Mn^{3+} and $S_2 = 3/2$ for Mn^{4+}). The shape of the magnetic peak of the specific heat (inset Fig. 2) seems to suggests that the transition is achieved in two steps, with a shoulder at 36 K and and a main peak at $T_N = 39$ K.

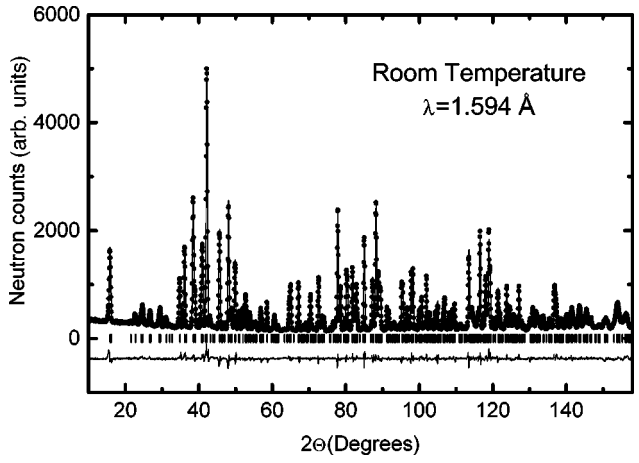

FIG. 3. Observed (solid circles), calculated (solid line), and difference (bottom line) NPD patterns. The tick marks correspond to the Bragg reflections of the orthorhombic space group *Pbam*.

IV. NEUTRON-DIFFRACTION MEASUREMENTS

A. Crystallographic structure

The crystal structure was refined from room-temperature D2B data, collected with a wavelength $\lambda = 1.594$ Å. All the Bragg reflections of the diagram were indexed with the lattice parameters $a = 7.560\,78(8)$ Å, $b = 8.532\,99(8)$ Å, and $c = 5.760\,66(5)$ Å. The pattern was refined in the space group *Pbam*, taking as starting structural model,[5] that of $LaMn_2O_5$. The good agreement between the calculated and observed patterns is presented in Fig. 3. The most characteristic parameters after the refinement are listed in Table I. A selection of the most important atomic distances and bonding angles are included in Tables II and III, respectively.

Figure 4 shows a view of the crystallographic structure along the *c* axis. Mn^{4+} (Mn1 atoms) are located within distorted octahedral environments. The $Mn^{4+}O_6$ octahedra form infinite linear chains along the *c* axis, sharing edges via O2 and O3 oxygens. Mn^{3+} cations are surrounded by five oxygens, forming $Mn^{3+}O_5$ distorted tetragonal pyramids. These units contain rather significantly different bond lengths: four oxygen atoms (two of O1 and two of O4) are in a square planar configuration and the fifth oxygen (O3) is in an axial position at a longer distance (2.085 Å). The pyramids interconnect the $Mn^{4+}O_6$ octahedra along the *c* axis via O3 and O4.

TABLE II. Selected interatomic distances at 295 K (in Å).

$Mn^{4+}O_6$		$Bi^{3+}O_8$	
Mn1-O2 (×2)	1.968(2)	Bi-O1 (×2)	2.488(1)
Mn1-O3 (×2)	1.870(2)	Bi-O2	2.374(2)
Mn1-O4 (×2)	1.910(1)	Bi-O2	2.353(2)
⟨Mn1-O⟩	1.916(2)	Bi-O4 (×2)	2.267(2)
$Mn^{3+}O_5$		Bi-O4 (×2)	2.785(2)
Mn2-O1 (×2)	1.899(2)	⟨Bi-O⟩	2.476(2)
Mn2-O3	2.085(3)	Mn1-Mn1	2.751(4)
Mn2-O4 (×2)	1.929(2)	Mn1-Mn1	3.010(4)
⟨Mn2-O⟩	1.948(3)	Mn2-Mn2	2.894(3)

TABLE III. Selected bonding angles at 295 K (in deg).

O2-Mn1-O2	80.2(2)	O1-Mn2-O1	80.7
O2-Mn1-O3	97.5(1)	O1-Mn2-O3	98.9(1)
O2-Mn1-O3	173.8(1)	O1-Mn3-O4	90.2(1)
O2-Mn1-O4	85.9(1)	O1-Mn2-O4	162.9(1)
O2-Mn1-O4	92.1(1)	O3-Mn2-O4	96.8(1)
O3-Mn1-O3	85.3(1)	O4-Mn2-O4	94.6(1)
O3-Mn1-O4	93.5(1)	Mn2-O1-Mn2	99.3(2)
O3-Mn1-O4	88.4(1)	Mn1-O2-Mn1	99.8(2)
O4-Mn1-O4	177.5(1)	Mn1-O3-Mn1	94.7(2)
		Mn1-O3-Mn2	131.2(2)
		Mn1-O4-Mn2	123.0(1)

The BiO_8 units can be described as bicapped trigonal prisms. It is noteworthy that they are significantly more distorted than the RO_8 units in other RMn_2O_2.[5] In particular, the two Bi-O4 distances (Table II) are much shorter (2.267 Å) or longer (2.785 Å), respectively, than the corresponding figures for other *R* members; for instance, La-O4 bond lengths are 2.496 Å and 2.562 Å, respectively. The distortion of the coordination environment is due to the presence of the electron lone pair on Bi^{3+}: the repulsion of the lone pair with Bi-O bonds leads to an asymmetric distribution of these bonds around Bi, involving significant shifts of some oxygen positions. Also, a coupled shift of the Bi position, by 0.15 Å along the direction [110] is observed with respect to the position of the rare-earth cations in other RMn_2O_5 oxides.[5] The mentioned oxygen shifts indirectly lead to important changes in Mn-O distances. In particular, $Mn1O_6$ octahedra show Mn1-O2 distances (1.968 Å) larger than any other members of the series. $Mn2O_5$ pyramids are also strongly affected, showing Mn2-O1 distances (1.899 Å) smaller and Mn2-O4 bond lengths (1.929 Å) larger that any other RMn_2O_5. These different interatomic distances will play an important role in the different spin arrangements along the *c* direction for $BiMn_2O_5$ with respect to those observed for other *R* cations.

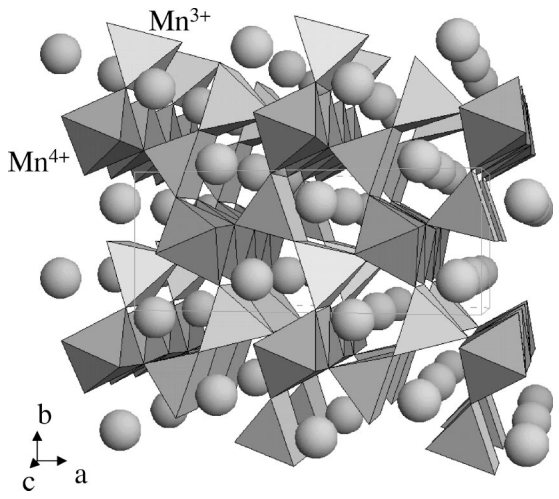

FIG. 4. A view of the crystallographic structure approximately along the *c* direction.

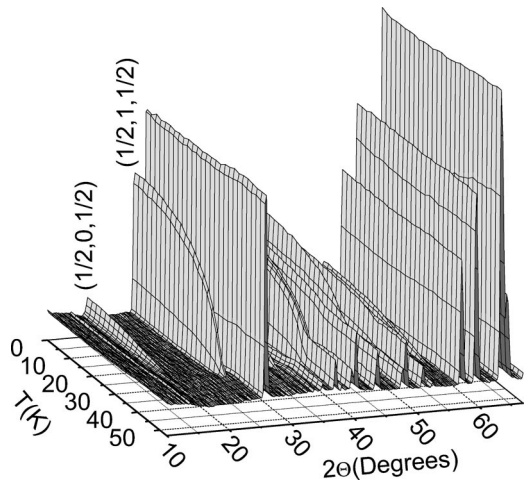

FIG. 5. Thermal variation of the NPD patterns acquired with $\lambda = 2.42$ Å in the temperature range $2 < T < 100$ K.

In a systematic study of RMn_2O_5 for *R* denoting rare-earth metals,[5] a regular increase of *a*, *b*, and c unit-cell parameters was found to correspond to the increase of the ionic radius of the R^{3+} cation along the series from Er to La. However, for $R = Bi^{3+}$, with an ionic radius of 1.20 Å, greater than that of La^{3+} ($r = 1.16$ Å), we have only observed an important increase in the *c* parameter [$c = 5.760\,66(5)$ Å for Bi versus 5.7214(1) Å for La (Ref. 5)], whereas the *a* parameter is close to that of Pr and *b* is similar to that of Eu. Again, the anisotropy observed in the Bi-O bond lengths, driven by the presence of the Bi^{3+} electron lone pair, is responsible for the anomalous variation of the unit-cell size.

B. Determination of the magnetic structure

The thermal evolution of the NPD patterns acquired in the temperature range $1.6 < T < 53.1$ K and with $\lambda = 2.532$ Å is shown in Fig. 5. Below $T \approx 40$ K, new diffraction peaks appear at scattering angles different from the Bragg positions corresponding to the space group *Pbam*. This confirms the appearance of a magnetic ordering below $T = 40$ K, in good agreement with the magnetic data. The magnetic reflections can be indexed by the propagation vector $\mathbf{k} = (1/2,0,1/2)$, which agrees with the results obtained in Ref. 10. Below the ordering temperature no anomalies are observed in the magnetic peaks, except an increase in the intensity on decreasing the temperature; therefore the magnetic structure seems to remain stable down to $T = 1.6$ K.

In the search of the possible magnetic structures, we have taken into consideration only those solutions (see the Appendix) that lead to equal magnetic moments for all the Mn atoms at the same site. All these solutions, given by the basis vectors presented in Table VII, have been contrasted with the experimental NPD data. The solution that gives a better agreement with the experimental results is $(F_x, C_y, 0)$ for the $4h$ site and $(G'_x, A'_y, 0)$ for the $4f$ site. The results of the fit carried out at $T = 1.6$ K are shown in Table IV. The agreement between calculated and experimental NPD patterns at 1.6 K is displayed in Fig. 6. According to the experimental

TABLE IV. Results from the magnetic structure determination at $T=1.6$ K.

	Mn($4h$)	Mn($4f$)
Solution	$(F_x,C_y,0)$	$(G'_x,A'_y,0)$
Values (μ_B)	$(-3.12(9),-0.8(2),0)$	$(2.44(10),0.6(2),0)$
$\lvert\mathbf{m}\rvert(\mu_B)$	3.23(6)	2.51(7)
Disc. factors	R_B(Nuc.)$=2.4\%$, R_B(Mag.)$=4.2\%$, $\chi^2=2.7$	

results the magnetic structure is given by the basis vectors of Γ_1, which corresponds to a magnetic structure with the moments oriented in the ab plane, as shown in Fig. 7. The thermal evolution of the magnetic moments at both Mn sites is displayed in Fig. 8. The values of the magnetic moments reach saturation below 5 K and, for both Mn sites, the orientation of the moments with respect to the a axis remains nearly constant below T_N. The magnetic moments at $T=1.6$ K are $3.23(6)\mu_B$ and $2.51(7)\mu_B$ for $4h$ and $4f$ sites, respectively. This result is concomitant with the different oxidation states exhibited by Mn cations at both crystallographic sites.

Let us point out that this solution, as has been explained in the Appendix, is equivalent to the solution $(C_x,F_y,0)$ for the $4h$ site and $(A'_x,G'_y,0)$ for the $4f$ site. On the other hand there is another solution, also belonging to Γ_1, that is in agreement with the experimental results, although the discrepancy factors are slightly worse. This solution is $(F_x,A_y,0)$ for the $4h$ site and $(G'_x,A'_y,0)$ for the $4f$ site, with the corresponding R_B (Magnet)$=6.8\%$.

V. DISCUSSION

Neutron-diffraction experiments have confirmed that $BiMn_2O_5$ presents an AFM ordering below $T_N=39$ K. The magnetic structure is commensurate with the chemical unit cell, with $\mathbf{k}=(1/2,0,1/2)$; the magnetic moments at the two crystallographically independent sites are very different, as should correspond to Mn cations in different oxidation states. Mn^{4+} cations at $4f$ sites are octahedrally coordinated, hence a t_{2g}^3 electronic configuration is expected ($S=3/2$). For Mn^{3+} cations (located at $4h$ sites) the corresponding electronic configuration in a pyramidal crystal field is $t_{2g}^3e_g^1$ ($S=2$). In both cases the saturation moments [$2.51(7)\mu_B$ and $3.23(6)\mu_B$, respectively] are slightly lower than those expected ($3\mu_B$ and $4\mu_B$, respectively), which can be due to covalency effects. The neutron-diffraction experiments, performed with a rather broad temperature aquisition step, did not allow us to clarify whether a small delay exists in the ordering temperatures of the Mn^{3+} and Mn^{4+} sublattices, which could explain the two characteristic temperatures observed in the anomaly of the susceptibility and specific-heat curves. However, the large difference in magnetic-moment values at both sites just below the ordering temperature, could be an indication that a small delay indeed takes place.

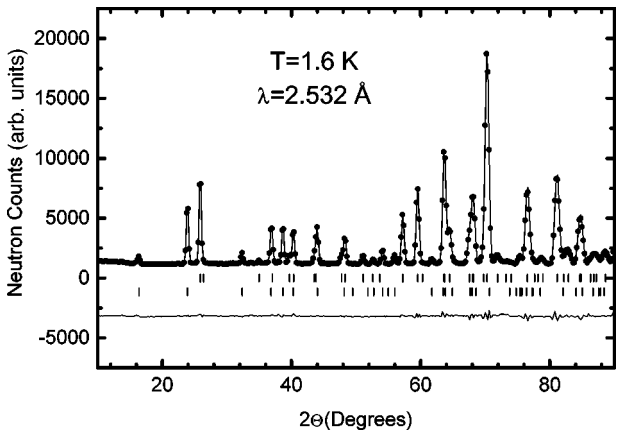

FIG. 6. Observed (solid circles), calculated (solid line), and difference (bottom line) NPD patterns corresponding to the solution $(F_x,C_y,0)$ for the $4h$ site and $(G'_x,A'_y,0)$ for the $4f$ site. The two series of tick marks correspond to the crystallographic and magnetic Bragg reflections.

As shown in Fig. 7, Mn^{4+} ions (labeled Mn1, $4f$ sites) are distributed in (001) planes forming a chain along the c axis: they are present at the $z=1-z_0$, $z=z_0$, and $z=-z_0$ planes ($z_0=0.261$). Intercalated between them, there are planes of Mn^{3+} ions at $z=1/2$. Also, we must consider the interleaved planes of Bi^{3+} ions at $z=0$. Thus, the $z=z_0$ and $z=-z_0$ Mn^{4+} planes are separated by a Bi^{3+} plane and the coupling between them is AFM; on the contrary, between the $z=1-z_0$ and $z=z_0$ Mn^{4+} planes, separated by a Mn^{3+} plane, the coupling is ferromagnetic (see Fig. 7). In the first case the distance between the Mn^{4+} planes is 3.010(4) Å and in the second case it is 2.751(4) Å. Within each Mn plane, for both Mn^{3+} and Mn^{4+} sublattices, the coupling along the b direction is ferromagnetic and along the a direction, it is AFM. In the Mn^{3+} planes, the ions related by an inversion center are antiferromagnetically coupled.

In both Mn^{3+} and Mn^{4+} sublattices, the superexchange

TABLE V. Irreducible representations of the space group $Pbam$ for $\mathbf{k}=(1/2,0,1/2)$. The symmetry elements are written according to Kovalev's notation. $\tau=(1/2,1/2,0)$.

	h_1	$h_2/(\tau)$	$h_3/(\tau)$	h_4	h_{25}	$h_{26}/(\tau)$	$h_{27}/(\tau)$	h_{28}
Γ_1	$\begin{pmatrix}1&0\\0&1\end{pmatrix}$	$\begin{pmatrix}0&1\\\bar{1}&0\end{pmatrix}$	$\begin{pmatrix}1&0\\0&\bar{1}\end{pmatrix}$	$\begin{pmatrix}0&1\\1&0\end{pmatrix}$	$\begin{pmatrix}0&1\\1&0\end{pmatrix}$	$\begin{pmatrix}1&0\\0&\bar{1}\end{pmatrix}$	$\begin{pmatrix}0&1\\\bar{1}&0\end{pmatrix}$	$\begin{pmatrix}1&0\\0&1\end{pmatrix}$
Γ_2	$\begin{pmatrix}1&0\\0&1\end{pmatrix}$	$\begin{pmatrix}0&1\\\bar{1}&0\end{pmatrix}$	$\begin{pmatrix}1&0\\0&\bar{1}\end{pmatrix}$	$\begin{pmatrix}0&1\\1&0\end{pmatrix}$	$\begin{pmatrix}0&\bar{1}\\\bar{1}&0\end{pmatrix}$	$\begin{pmatrix}\bar{1}&0\\0&1\end{pmatrix}$	$\begin{pmatrix}0&\bar{1}\\1&0\end{pmatrix}$	$\begin{pmatrix}\bar{1}&0\\0&\bar{1}\end{pmatrix}$

TABLE VI. Basis vectors.

	Mn($4h$)	Mn($4f$)	
Γ_1	$V_1^x=\begin{pmatrix} m_{1x}+m_{3x} & m_{2x}+m_{4x} \\ m_{2x}-m_{4x} & m_{1x}-m_{3x} \end{pmatrix}$	$V_1'^x=\begin{pmatrix} G_x' & G_x' \\ A_y' & A_y' \end{pmatrix}$	$V_1'^y=\begin{pmatrix} A_y' & A_y' \\ G_y' & G_y' \end{pmatrix}$
	$V_1^y=\begin{pmatrix} m_{1y}-m_{3y} & m_{2y}-m_{4y} \\ m_{2y}+m_{4y} & m_{1y}+m_{3y} \end{pmatrix}$	$V_1'^z=\begin{pmatrix} C_z' & C_z' \\ F_z' & F_z' \end{pmatrix}$	
Γ_2	$V_2^z=\begin{pmatrix} m_{1z}+m_{3z} & m_{2z}+m_{4z} \\ m_{2z}-m_{4z} & m_{1z}-m_{3z} \end{pmatrix}$	$V_2'^x=\begin{pmatrix} C_x' & C_x' \\ F_x' & F_x' \end{pmatrix}$	$V_2'^y=\begin{pmatrix} F_y' & F_y' \\ C_y' & C_y' \end{pmatrix}$
		$V_2'^z=\begin{pmatrix} G_z' & G_z' \\ A_z' & A_z' \end{pmatrix}$	

interaction among the Mn ions takes place via the O^{2-} ions; within the Mn^{4+} planes, O1 and O4 oxygens are responsible for superexchange; in the Mn^{3+} planes the O3 oxygens are involved in this process. In both cases the Mn-O distances along the *b* axis are greater than those observed along the *a* axis. This fact would explain that the superexchange interactions between closer neighbors along the *b* axis is ferromagnetic whereas along the *a* axis it is AFM. Along the chains of $Mn^{4+}O_6$ octahedra, we observe different interactions between Mn^{4+} planes separated by Bi^{3+} planes and those separated by Mn^{3+} planes, as commented above. In the first case, the direct Mn^{4+}-O-Mn^{4+} interaction results are AFM. In the second case, it must be considered as an admixture of a direct interaction between the Mn^{4+} planes (Mn^{4+}-O-Mn^{4+}, labeled J_1) and an indirect interaction through the Mn^{3+} ions (Mn^{4+}-O-Mn^{3+}-O-Mn^{4+}, labeled J_2). The J_1 direct interaction would be AFM; the indirect interaction Mn^{4+}-O-Mn^{3+}, J_2, is also AFM and it seems to predominate in such a way that the final coupling between Mn^{4+} cations at z_0 and $1-z_0$ planes is ferromagnetic. Summarizing, Mn^{4+} magnetic moments are alternatively ferromagnetically and antiferromagnetically coupled, along the *c* axis, the moments always remaining on the *ab* plane.

The magnetic structure of $BiMn_2O_5$ is different from those of the other members of the RMn_2O_5 family (R = rare earths): it is defined by the commensurate propagation vector $\mathbf{k}=(1/2,0,1/2)$, whereas for the other members of the family the magnetic structure is incommensurate along the *c* axis, with $\mathbf{k}=(1/2,0,\tau)$, as shown in Fig. 9. In $BiMn_2O_5$, the above-mentioned Mn^{4+}-O-Mn^{3+}-O-Mn^{4+} indirect interaction (i.e., the coupling between Mn^{4+} neighbors via bridging Mn^{3+} cations) predominates, in such a way that the final coupling between the Mn^{4+} planes separated by Mn^{3+} planes is purely ferromagnetic. The commensurability of the structure is directly related to this pure ferromagnetic interaction between couples of Mn^{4+} neighbors. In other members of the family, as in $ErMn_2O_5$, $HoMn_2O_5$, and $NdMn_2O_5$, the moments of those Mn^{4+} couples form a certain angle (different from zero and always on the *ab* plane), implying the incommensurability of the magnetic structure. The imperfect parallelism between these moments indicates a competition between the direct (Mn^{4+}-O-Mn^{4+}) an indirect Mn^{4+}-O-Mn^{3+}-O-Mn^{4+} superexchange interactions, i.e., between J_1 and J_2. The relative strength of both inter-

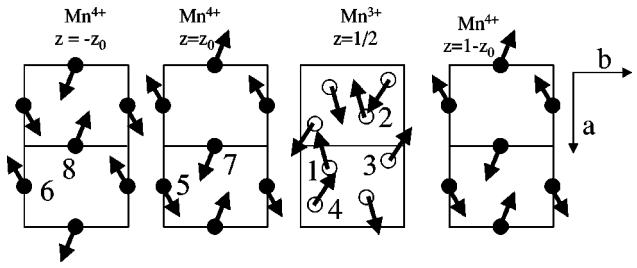

FIG. 7. Schematic view of the magnetic structure, along successive Mn planes (*c*-axis direction).

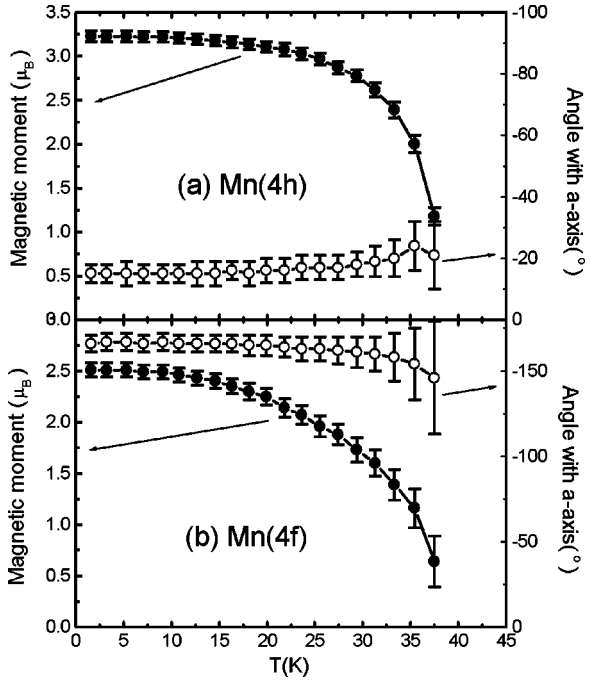

FIG. 8. Thermal variation of the magnetic moments and the angle with respect to the *a* axis below T_N (a) for the Mn atoms at $4h$ site and (b) for the Mn atoms at $4f$ site.

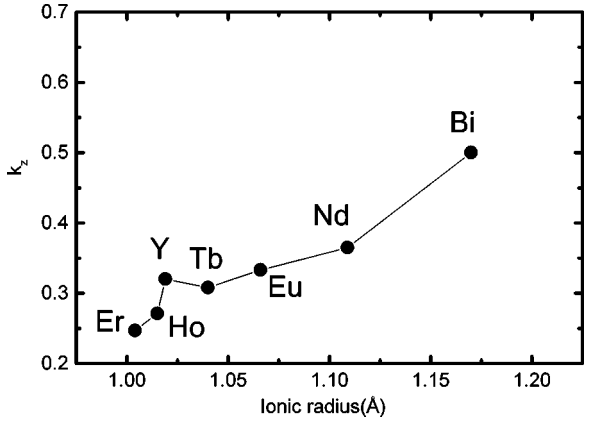

FIG. 9. Evolution of the k_z component of the propagation vector $\mathbf{k}=(1/2,0,k_z)$ as a function of the R^{3+} ionic radius (in eightfold coordination) for the $R\mathrm{Mn_2O_5}$ family. Ionic radii are taken from Ref. 15 and k_z from Refs. 6–9.

actions is certainly related to the concerned Mn-O-Mn distances. In the previous structural part, we described that Mn^{4+} cations are linked by O2 and O3 oxygens along the c direction, and two Mn^{4+} neighbors are also linked together by Mn^{3+} cations via O3 and O4 oxygens. We commented that in $BiMn_2O_5$, Mn^{4+}-O2 distance is larger than in any other member of the $R\mathrm{Mn_2O_5}$ series; this means a weaker AFM direct coupling along the chains (weak J_1), in such a way that the indirect (Mn^{4+}-O-Mn^{3+}-O-Mn^{4+}) coupling predominates ($J_2>J_1$), but only for $BiMn_2O_5$; for the remaining $R\mathrm{Mn_2O_5}$ members the shortening of the crucial Mn^{4+}-O2 bond lengths means a strengthening of the direct AFM interactions between Mn^{4+} couples ($J_1\approx J_2$). The competition between the AFM direct (J_1) and indirect (J_2) interactions gives rise to an imperfect alignment of Mn^{4+} magnetic moments and to the incommensurability of the structure. Figure 9 shows the evolution of the k_z component of the propagation vector $\mathbf{k}=(1/2,0,k_z)$ in terms of the ionic radius for $R\mathrm{Mn_2O_5}$ according to the data presented in Ref. 6; k_z decreases for the smaller rare-earth metals, since the reduction in size of the R^{3+} cation is concomitant with the shortening of the $\langle$Mn1-O$\rangle$ distances, thus increasing the value of the J_1 direct AFM interaction term along the chains of Mn1-O_6 octahedra.

VI. CONCLUSIONS

Neutron-diffraction measurements have confirmed that the perovskite-related compound $BiMn_2O_5$ orders below $T_N=39$ K, with a noncollinear commensurate magnetic structure characterized by the propagation vector $\mathbf{k}=(1/2,0,1/2)$. The moments of the Mn^{3+} ions, located at the $4h$ sites, are ordered according to the basis vectors $(F_x,C_y,0)$, whereas for Mn^{4+} ions, placed at the $4f$ sites, the basis vectors are $(G'_x,A'_y,0)$. Mn^{4+} ions are distributed in (001) planes forming infinite chains along the c axis and are intercalated, either by Bi^{3+} planes or by Mn^{3+} planes. In the first case the coupling between the moments of the Mn^{4+} planes is AFM whereas in the second one it is ferromagnetic; thus FM and AFM couplings alternate along the chains of $Mn^{4+}O_6$ octahedra. The commensurability of the magnetic structure of $BiMn_2O_5$ is understood in terms of the concerned Mn^{4+}-O-Mn^{4+} distances; in couples of Mn^{4+} cations bridged by Mn^{4+}-O-Mn^{3+}-O-Mn^{4+} paths, a perfect FM ordering between these couples is provided by the relative weakness of the direct Mn^{4+}-O-Mn^{4+} superexchange interactions. For the remaining terms of the $R\mathrm{Mn_2O_5}$ series, the progressive shortening of direct Mn^{4+}-O-Mn^{4+} bond lengths, enhancing the direct AFM interactions, accounts for the observed incommensurability of the magnetic structures along the c-axis direction.

ACKNOWLEDGMENTS

We thank the financial support of CICyT to the Projects Nos. MAT2001-0539 and MAT99-1045 and we are grateful to ILL for making all facilities available.

APPENDIX: GROUP THEORY ANALYSIS

The possible magnetic structures compatible with the symmetry of $BiMn_2O_5$ are determined by following the representation analysis technique described by Bertaut.[16] For the propagation vector $\mathbf{k}=(1/2,0,1/2)$, the small group $G_\mathbf{k}$, formed by those elements of the space group that leave $\mathbf{k}$ invariant, coincides with the space group $Pbam$. For $\mathbf{k}=(1/2,0,1/2)$, the irreducible representations of the group $G_\mathbf{k}$ are those shown in Table V, which have been taken from Ref. 17. In the Kovalev's tables[17] only the irreducible representations of the point group $g_\mathbf{k}$ appear, which is constructed from the group $G_\mathbf{k}$ by only taking into consideration the rotational part of the elements of symmetry. The irreducible representations of $G_\mathbf{k}$ are obtained from those given by Kovalev through the expression $\zeta_{\mathbf{k}\nu}(h_i/\tau)=\exp(-i\mathbf{k}\tau)\gamma_{\mathbf{k}\nu}(h_i)$. The two-dimensional irreducible representations obtained in this way are complex, and they have been transformed into real through a unitary transformation by using the matrix

$$A=\frac{1}{2}\begin{pmatrix} i & 1 \\ 1 & i \end{pmatrix}. \tag{A1}$$

The irreducible representations $\Gamma_\mathbf{k}$ shown in Table V are determined from $\zeta_{\mathbf{k}\nu}$ by means of the transformation $\Gamma_{\mathbf{k}\nu}=A\zeta_{\mathbf{k}\nu}A^{-1}$. A representation Γ is then constructed with the Fourier components $\mathbf{m}^\mathbf{k}$ corresponding to the Mn atoms of each site. The Mn atoms at the $4h$ site are denoted as (1) $(x,y,1/2)$, (2) $(-x,-y,1/2)$, (3) $(-x+1/2,y+1/2,1/2)$, and (4) $(x+1/2,-y+1/2,1/2)$. The Mn atoms at the $4f$ site are numbered as (5) $(1/2,0,z)$, (6) $(1/2,0,-z)$, (7) $(0,1/2,z)$, and (8) $(0,1/2,-z)$. The decomposition of the representation Γ in terms of the irreducible representations of $\Gamma_\mathbf{k}$ is for the $4h$ site,

$$\Gamma(4h)=4\Gamma_1+2\Gamma_2, \tag{A2}$$

and for the $4f$ site,

$$\Gamma(4f)=3\Gamma_1+3\Gamma_2. \tag{A3}$$

TABLE VII. Basis vectors with equal magnetic moments for the atoms of the $4h$ site.

	Mn($4h$)				Mn($4f$)		
Γ_1	$\begin{pmatrix}F_x\\C_x\end{pmatrix}$	$\begin{pmatrix}G_x\\A_x\end{pmatrix}$	$\begin{pmatrix}C_y\\F_y\end{pmatrix}$	$\begin{pmatrix}A_y\\G_y\end{pmatrix}$	$\begin{pmatrix}G'_x\\A'_x\end{pmatrix}$	$\begin{pmatrix}A'_y\\G'_y\end{pmatrix}$	$\begin{pmatrix}C'_z\\F'_z\end{pmatrix}$
Γ_2		$\begin{pmatrix}F_z\\C_z\end{pmatrix}$	$\begin{pmatrix}G_z\\A_z\end{pmatrix}$		$\begin{pmatrix}C'_x\\F'_x\end{pmatrix}$	$\begin{pmatrix}F'_y\\C'_y\end{pmatrix}$	$\begin{pmatrix}G'_z\\A'_z\end{pmatrix}$
$\mathbf{F}=\mathbf{m}_1+\mathbf{m}_2+\mathbf{m}_3+\mathbf{m}_4$		$\mathbf{G}=\mathbf{m}_1-\mathbf{m}_2+\mathbf{m}_3-\mathbf{m}_4$		$\mathbf{F}'=\mathbf{m}_5+\mathbf{m}_6+\mathbf{m}_7+\mathbf{m}_8$		$\mathbf{G}'=\mathbf{m}_5-\mathbf{m}_6+\mathbf{m}_7-\mathbf{m}_8$	
$\mathbf{C}=\mathbf{m}_1+\mathbf{m}_2-\mathbf{m}_3-\mathbf{m}_4$		$\mathbf{A}=\mathbf{m}_1-\mathbf{m}_2-\mathbf{m}_3+\mathbf{m}_4$		$\mathbf{C}'=\mathbf{m}_5+\mathbf{m}_6-\mathbf{m}_7-\mathbf{m}_8$		$\mathbf{A}'=\mathbf{m}_5-\mathbf{m}_6-\mathbf{m}_7+\mathbf{m}_8$	

The different basis vectors associated with each irreducible representation and calculated by following the projection operator technique, are presented in Table VI. Regarding the basis vectors corresponding to the $4h$ site, there is a relationship between the atoms (1) and (3) and between (2) and (4); therefore solutions with different magnetic moments for both groups of atoms are possible. On the contrary, all the solutions belonging to the $4f$ site imply the same magnetic moment for all of the Mn atoms. The basis functions given for the $4h$ site would lead to solutions with equal moment in case the matrix elements of each basis function V_i^α verify

$$V_i^\alpha(11)=V_i^\alpha(12) \quad \text{or} \quad V_i^\alpha(11)=-V_i^\alpha(12) \tag{A4}$$

or

$$V_i^\alpha(21)=V_i^\alpha(22) \quad \text{or} \quad V_i^\alpha(21)=-V_i^\alpha(22). \tag{A5}$$

The basis vectors finally obtained are shown in Table VII. Let us point out that some of the possible solutions are equivalent. For instance, in the case of Γ_1, a solution such as $(F_x,A_y,0)$ for the $4h$ site plus $(F'_x,G'_y,0)$ for the $4f$ site is equivalent to the solution $(C_x,G_y,0)$ plus $(C'_x,A'_y,0)$. It is due to the fact that the amounts $F_xA_y+C_xG_y$, $F_xF'_x+C_xC'_x$ and $A_yG'_y+G_yA'_y$ are invariant. The symmetry elements h_i/τ with $i=1$, 3, 26, and 28 transform each basis vector into itself, whereas h_i/τ with $i=2$, 4, 25, and 27 transforms **F** into **C** and vice versa, and **G** into **C** and vice versa.

*Email address: amunoz@fis.uc3m.es

[1] R.M. Kusters, J. Singleton, D.A. Keen, R. McGreevy, and W. Hayes, Physica B **155**, 362 (1989).
[2] R. Von Helmolt, J. Wecker, B. Holzapfet, L. Schultz, and K. Samwer, Phys. Rev. Lett. **71**, 2331 (1993).
[3] S. Quezel-Ambrunaz, E.F. Bertaut, and G. Buisson, C. R. Acad. Sci. **258**, 3025 (1964).
[4] E.F. Bertaut, G. Buisson, A. Durif, A. Mareschal, M.C. Montmory, and S. Quezel-Ambrunaz, Bull. Soc. Chim. Fr. **1965**, 1132.
[5] J.A. Alonso, M.T. Casais, M.J. Martínez-Lope, J.L. Martínez, and M.T. Fernández-Díaz, J. Phys.: Condens. Matter **9**, 8515 (1997).
[6] G. Buisson, Phys. Status Solidi A **16**, 533 (1973).
[7] G. Buisson, Phys. Status Solidi A **17**, 191 (1973).
[8] P.P. Gardner, C. Wilkinson, J.B. Forsyth, and B.M. Wanklyn, J. Phys. C **21**, 5653 (1988).
[9] C. Wilkinson, F. Sinclair, P.P. Gardner, J.B. Forsyth, and B.M. Wanklyn, J. Phys. C **14**, 1671 (1981).
[10] E.F. Bertaut, G. Buisson, S. Quezel-Ambrunaz, and G. Quezel, Solid State Commun. **5**, 25 (1967).
[11] H. Tsujino, Y. Tanaka, and K. Kohn, in Proceedings of the 6th International Conference on Ferrites, Tokyo and Kyoto, 1992, edited by M. Abe and T. Yamaguchi.
[12] K. Saitoand K. Kohn, J. Phys.: Condens. Matter **7**, 2855 (1995).
[13] A. Inomata and K. Kohn, J. Phys.: Condens. Matter **8**, 2673 (1996).
[14] J. Rodríguez-Carvajal, Physica B **192**, 55 (1993).
[15] R.D. Shannon, Acta Crystallogr., Sect. A: Cryst. Phys., Diffr., Theor. Gen. Crystallogr. **A32**, 751 (1976).
[16] E.F. Bertaut, in *Magnetism*, edited by G.T. Rado and H. Shul (Academic, New York, 1963), Vol. III, Chap. 4.
[17] O.K. Kovalev, in *Representation of the Crystallographic Space Group*, edited by H.T. Stokes and D.M. Hatch, 2nd ed. (Gordon and Breach, New York, 1993).